Progress In Electromagnetics Research B, Vol. 81, 25–44, 2018

Analytical Model of the Magnetic Field Distribution of a Generator Combined with Magnetic Bearing in Wind Turbines

Yanjun Yu*, Qianwen Xiang, Xinhua Zhang, and Weiyu Zhang

Abstract—To achieve radial suspension and eliminate the effect of rotor gravity in wind turbines, a novel structure of a generator combined with a magnetic bearing (GCWMB) is proposed in this paper. The GCWMB not only has the characteristics of the traditional permanent magnet (PM) generator but also has the advantages of reducing friction and starting wind speed, eliminating rotor gravity. The structure and principle of the GCWMB are analyzed in this paper. To improve the calculation accuracy of flux density, an analytical model based on the Fourier series decomposition is proposed to establish the model of flux density in the outer air gap. Taking into account the edge effects and the eccentricity of the rotor, an improved equivalent magnetic circuit method is adopted to model and analyze the flux density in the inner air gap. The effectiveness and correctness of the proposed analytical model in the outer and inner air gaps are verified by finite element analysis (FEA) and experiments.

1. INTRODUCTION

Wind turbines, with the advantages of endless resources, low cost and convenient use, have become one of the most promising new energy technologies and are a mature technology implemented at a large scale [1–3]. Traditional wind turbines are supported by mechanical bearings, which have many shortcomings, such as high starting speed, large starting torque, high maintenance cost, low utilization rate of wind energy, short life of rolling bearing and so on; these shortcomings have seriously restricted the development of wind turbine technology [4, 5].

Magnetic bearings are high-performance bearings that use magnetic force to suspend the rotor in space without mechanical contact between the rotors and the stators [6, 7]. At present, the most widely structures of magnetic bearings are mainly composed of three types: passive magnetic bearings, active magnetic bearings and hybrid magnetic bearings [8, 9]. Hybrid magnetic bearings have the advantages of active magnetic bearings and passive magnetic bearings, in which the bias magnetic fluxes are provided by PMs, thereby reducing both the number of turns of coils and the power consumption [10, 11]. The application of magnetic bearings for wind turbines can effectively reduce the starting speed, noise, failure rate of the spindle and friction [12, 13].

Halbach arrays of magnetized rotors offer several attractive features. For example, the air gap field distribution using a Halbach array is inherently sinusoidal, and the cogging torque may be negligible; as a result, the power density will be increased because of the higher working point of the magnet. Because of the self-shielding magnetization, the rotor back-iron is not essential, thereby enabling the mass and inertia to be reduced [14, 15]. Because of the above mentioned advantages, Halbach magnetized PM machines are widely used in various applications [16].

To achieve the advantages of two objects at once, many scholars have combined two objects into a single object. For example, a magnetic-geared PM motor consists of a magnetic gear and a PM motor [17, 18]. A bearingless motor consists of a magnetic bearing and a motor [19]. A double stator

---

Received 27 March 2018, Accepted 17 May 2018, Scheduled 30 May 2018

* Corresponding author: Yanjun Yu (yuyanjun@ujs.edu.cn).
The authors are with the School of Electrical and Information Engineering, Jiangsu University, Zhenjiang 212013, China.

type bearingless switched reluctance motor consists of a magnetic bearing and a switched reluctance motor [20]. Thus, a Halbach magnetized PM generator and a magnetic bearing eliminating rotor gravity are combined in this paper.

As well known, the magnetic field distribution in the air gap is the key factor of analysis, design and optimization in machines. Therefore, it is necessary to establish an accurate analytical model of the magnetic field distribution in the air gap. In recent years, much progress has been made in analytical models, e.g., equivalent magnetic circuit method, finite element method, magnetic-charge method, and Fourier series decomposition method [21–23]. The equivalent magnetic circuit method transforms the nonuniform magnetic field in space into some multi-section magnetic circuits. The finite element method has high calculation accuracy, but the calculation cycle is the longest. The magnetic-charge method, which can be solved easily with the numerical integration, is mainly used to calculate the magnetic field of the PMs' edges [24]. Fourier series decomposition using the harmonic model of a double Fourier series can accurately describe the magnetic field distribution of each part in machines.

The remainder of this paper is organized as follows. The structure and operational principle of the GCWMG, which can eliminate rotor gravity, are proposed in Section 2. In Section 3, the analytical model of flux density in the outer air gap is established. Next, magnetic field computations for the inner air gap according to an improved magnetic field analytical method are deduced in Section 4. In Section 5, simulations and experiments are conducted to verify the analytical models and the correctness of GCWMG. Finally, the conclusion is given in Section 6.

2. STRUCTURE AND PRINCIPLE OF A NOVEL GCWMG

2.1. Structure of the GCWMG

To shorten the axial length of wind turbines, increase the utilization of wind energy and eliminate the effects of rotor gravity, a novel maglev wind turbine is proposed in this paper. The structure of a maglev wind turbine system (shown in Fig. 1) mainly includes a GCWMG, a spare bearing, and blades. The GCWMG combines a magnetic bearing and a Halbach magnetized PM generator; this combination not only can achieve the functions of suspension and power generation but also eliminate the effects of rotor gravity.

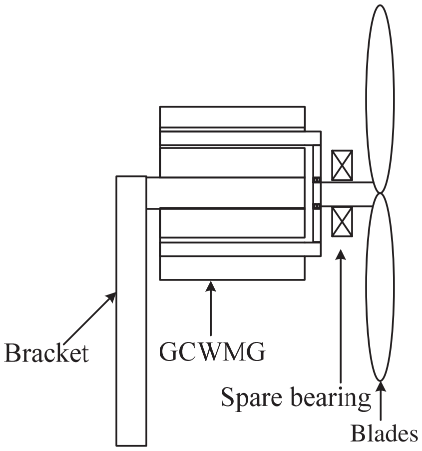

Figure 1. Structure of a maglev wind turbine.

The proposed GCWMG is shown in Fig. 2(a); the GCWMG includes an inner stator, an outer stator, a distributed hollow rotor, armature windings, suspension control windings, and PMs and so on. The inner stator contains a total of 7 poles: two bias flux poles, one pole of eliminating rotor gravity, and four suspension control poles. Two radial magnetized PMs are placed on the surface of bias flux poles, and four suspension windings are wound around the suspension control poles. To obtain an ideal sinusoidal distribution of the magnetic field in the air gap and reduce the radial rotor thickness,

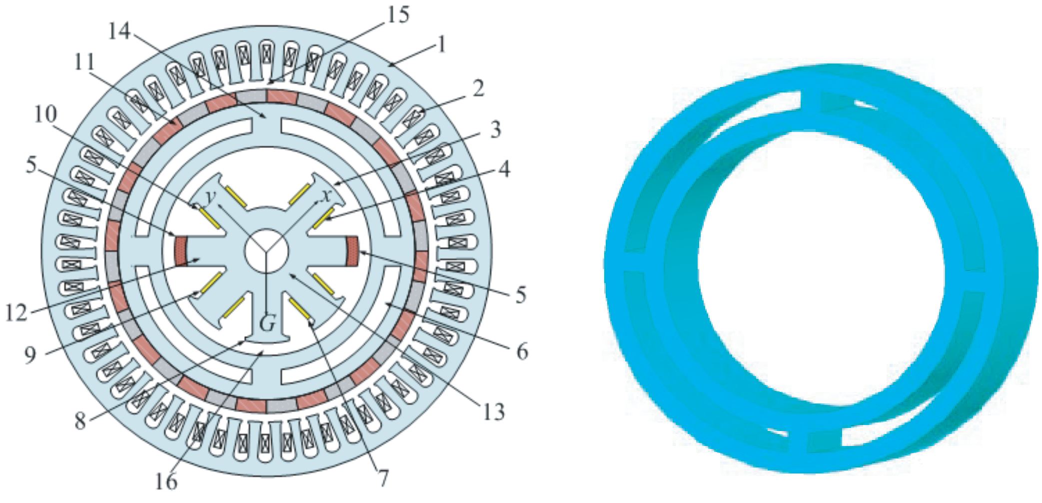

(a) (b)

Figure 2. Structure and three dimensional graph of the GCWMG. (a) Structure of the GCWMG. (b) Three dimensional graph of the distributed hollow rotor. 1 — outer stator; 2 — armature windings; 3 — suspension control pole; 4 — suspension control windings in $+x$ direction; 5 — permanent magnet; 6 — hollow part of rotor; 7 — suspension control windings in $-y$ direction; 8 — eliminating rotor gravity pole; 9 — suspension control windings in $-x$ direction; 10 — suspension control windings in $+y$ direction; 11 — Halbach array; 12 — bias flux pole; 13 — inner stator; 14 — rotor; 15 — outer air gap; 16 — inner air gap.

a Halbach magnetized permanent-magnet array is placed on the outer surface of the rotor. According to [25], the maximum deflection will most likely occur in the middle of the rotor. Thus, to improve the stiffness of rotor, the distributed hollow structure is used in the rotor. The three-dimensional graph of the distributed hollow rotor is shown in Fig. 2(b).

2.2. Principle of Eliminating Rotor Gravity in the GCWMG

In the traditional magnetic bearings, the suspension force is produced by suspension windings to overcome the effects of rotor gravity. As a result, the power loss of magnetic bearings is increased [26]. In addition, the effects of rotor gravity in magnetic bearings were not considered in some literature studies, resulting in errors in the control [27]. To decrease the power loss, the GCWMG, which can offset rotor gravity without additional control currents, is proposed in this paper. The schematic diagram of the process of eliminating rotor gravity is shown in Fig. 3.

To illustrate the principle of eliminating rotor gravity, the x and y directions and gravity direction (G direction) are set in this paper. The bias flux Φ_{pm} generated by two radial magnetized PMs is shown as the solid lines in Fig. 3. The bias flux passes through inner air gap, rotor, inner stator then returns back to the PMs.

Supposing that the rotor is suspended in the equilibrium position, the flux density amplitudes of air gap in the x and y directions are the same, and there is no current in the suspension control windings at this moment. The flux density distribution in the G direction is nonuniform because there is only one pole of eliminating rotor gravity in the $+G$ direction. Thus, the amplitude of flux density in $+G$ direction is larger than the amplitude in the $-G$ direction. According to Maxwell theory, a Maxwell force that is opposite to the gravity will be generated on the rotor surface [28]. If the above Maxwell force is set to be equal to the rotor gravity, then the rotor will be suspended in the equilibrium position without adding any suspension control currents. As a result, the power loss of the GCWMG will be decreased.

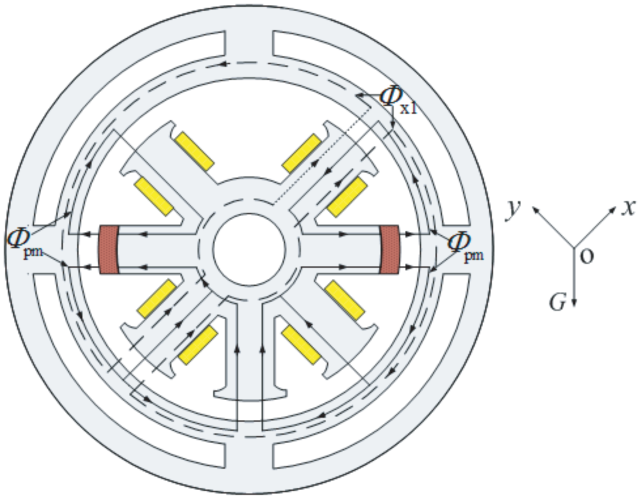

Figure 3. Schematic diagram of eliminating rotor gravity via electromagnetic forces on the rotor.

2.3. Principle of Suspension Control in the GCWMG

In the common state, the rotor can be suspended in the equilibrium position, and there is no suspension control current in the GCWMG. Taking the x direction as an example, as the rotor is shifted to $-x$ direction by disturbance, the length of the inner air gap in the $-x$ direction will be larger than length of inner air gap in the $+x$ direction. Thus, the flux density of inner air gap in the $-x$ direction will be smaller than the flux density of the inner air gap in the $+x$ direction.

To cause the rotor to return to the equilibrium position, the suspension control currents are added to the corresponding control windings in the $+x$ and $-x$ directions. Thus, the control flux Φ_{x1} will be generated in the inner air gap, as shown by the dotted lines in Fig. 3. At this time, the control flux Φ_{x1} will add the bias flux Φ_{pm} in the $-x$ direction and subtract Φ_{pm} in the $+x$ direction, leading to the flux density amplitude of the inner air gap in the $-x$ direction being larger than the amplitude in the $+x$ direction. According to Maxwell theory, the Maxwell force F along the $+x$ direction will be generated on the rotor. As a result, the rotor will be pulled back to the equilibrium position. The principle of the suspension control in the radial y direction is the same as above. Therefore, the rotor can be stably suspended in the radial 2-DOF direction by controlling the suspension control currents.

Based on the above analysis, it can be seen that the GCWMG not only has the characteristics of the traditional PM generator but also has the advantages of reducing the friction and the starting wind speed as well as eliminating rotor gravity.

3. ANALYTICAL MODEL IN THE OUTER AIR GAP

3.1. Basic Theory of the Magnetic Field Analytical Method

The magnetic field distribution of the outer air gap is very complex because the Halbach magnetized permanent-magnet array is placed on the outside of the rotor. Fourier series decomposition, which can obtain the solutions of Laplace/Poisson equations and improve the calculation accuracy, is used to establish the analytical model in the outer air gap. In addition, the equivalent magnetic circuit method is used to establish the magnetic circuit model in the inner air gap, where there is an aperiodic variation in the inner air gap because only two radial magnetized PMs are mounted on the inner stator.

The number of poles $p = 1$ is not considered in this paper because the GCWMG is used in wind turbines. Moreover, the models established in this paper are solved in polar coordinates. Moreover, for simplicity, several assumptions are made as follows: 1) The permeabilities of iron are infinite. 2) The end effects and slotting are ignored. 3) The demagnetization curve of the PM is linear. 4) The size of each Halbach magnetized permanent-magnet array is the same, and the gap between each PM is ignored.

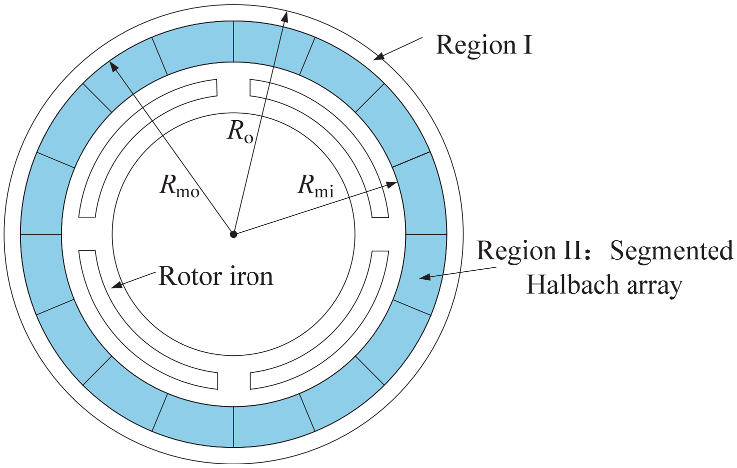

Figure 4. Symbols and subregions of the GCWMG outside the rotor.

To establish the analytical model of the magnetic field in the outer air gap, the calculation regions in the GCWMG outside the rotor can be divided into two subdomains (as shown in Fig. 4): the outer air gap (Region I) and the Halbach magnetized permanent-magnet array (Region II). R_o, R_{mo}, and R_{mi} are the outer radius of the outer air gap, the outer radius of the PMs and the inner radius of the PMs, respectively. The magnetization characteristics in two subdomains are described as below:

$$\text{In Region I}: \quad \mathbf{B}_1 = \mu_0 \mathbf{H}_1 \tag{1}$$

$$\text{In Region II}: \quad \mathbf{B}_2 = \mu_0 \mu_r \mathbf{H}_2 + \mu_0 \mathbf{M} \tag{2}$$

where $\mathbf{B}_1$ and $\mathbf{H}_1$ are the flux density and the field intensity in Region I, respectively. $\mathbf{B}_2$, $\mathbf{H}_2$, and $\mathbf{M}$ are the flux density, the field intensity and the residual magnetization vector of PMs in Region II, respectively. μ_r and μ_0 are the relative permeability and the air permeability of the magnets, respectively. The amplitude of the magnetization vector of the PM is

$$M = \frac{B_r}{\mu_0} \tag{3}$$

where B_r is the residual magnetic density of the magnets.

The magnetization vector of the PMs can be expressed in polar coordinates as follows:

$$\mathbf{M} = M_r \mathbf{r} + M_\theta \boldsymbol{\theta} \tag{4}$$

where M_r and M_θ are the components of radial magnetization and tangential magnetization, respectively.

Using the scalar magnetic potential, the governing equations of the no-load magnetic field in the subdomains satisfy the following relationships:

1) The scalar magnetic potential φ_1 in Region I is governed by the Laplace equation:

$$\nabla^2 \varphi_1 = \frac{\partial^2 \varphi_1}{\partial r^2} + \frac{1}{r}\frac{\partial \varphi_1}{\partial r} + \frac{1}{r^2}\frac{\partial^2 \varphi_1}{\partial \theta^2} = 0, \quad R_{mo} < r < R_o \tag{5}$$

2) The scalar magnetic potential φ_2 in Region II is governed by the Poisson equation:

$$\nabla^2 \varphi_2 = \frac{\partial^2 \varphi_2}{\partial r^2} + \frac{1}{r}\frac{\partial \varphi_2}{\partial r} + \frac{1}{r^2}\frac{\partial^2 \varphi_2}{\partial \theta^2} = \frac{\text{div}\mathbf{M}}{\mu_r}, \quad R_{mi} < r < R_{mo} \tag{6}$$

$$\text{div}\mathbf{M} = \frac{M_r}{r} + \frac{\partial M_r}{\partial r} + \frac{1}{r}\frac{\partial M_\theta}{\partial \theta} \tag{7}$$

The relations of the scalar magnetic potential and the field intensity of machines in polar coordinates are as follows:

$$\mathbf{H} = -\nabla \varphi \tag{8}$$

$$H_r = -\frac{\partial \varphi}{\partial r} \tag{9}$$

$$H_\theta = -\frac{1}{r}\frac{\partial \varphi}{\partial \theta} \tag{10}$$

The boundary conditions of the GCWMG are described below:

1) The tangential components of **H** on the contact surfaces in the GCWMG can be described as follows:

$$H_{1\theta}\left|_{r=R_O}\right. = 0 \tag{11}$$

$$H_{2\theta}\left|_{r=R_{mi}}\right. = 0 \tag{12}$$

2) The flux density **B** and the field intensity **H** on the contact surface between the outer air gap and the PMs can be described as follows:

$$B_{1r}\left|_{r=R_{mo}}\right. = B_{2r}\left|_{r=R_{mo}}\right. \tag{13}$$

$$H_{1\theta}\left|_{r=R_{mo}}\right. = H_{2\theta}\left|_{r=R_{mo}}\right. \tag{14}$$

Thus, the flux density of outer air gap in GCWMG can be solved according to the boundary conditions and the relationships between the flux density and the field intensity.

3.2. Calculation of the Residual Magnetization Vector in the PMs

The parallel magnetization method is often used in a Halbach magnetized permanent-magnet array. In addition, each PM in the array is magnetized according to the desired orientation. A schematic diagram of the magnetizing direction in the GCWMG is shown in Fig. 5.

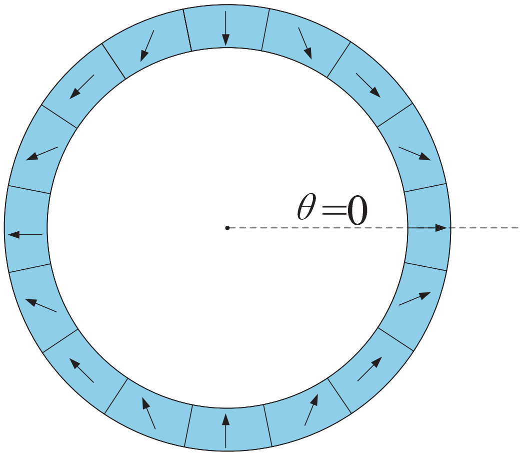

Figure 5. Schematic diagram of the magnetizing direction of the Halbach array in the GCWMG.

The residual magnetization vector $\mathbf{M}_i$ in the ith PM in polar coordinates can be expressed as below:

$$\mathbf{M}_i = \begin{bmatrix} M_{ri} \\ M_{\theta i} \end{bmatrix} = M \begin{bmatrix} \cos(\theta - \theta_{mi}) \\ -\sin(\theta - \theta_{mi}) \end{bmatrix} \tag{15}$$

The expression of θ_{mi}, which is the angle between $\theta = 0$ and the magnetization vector M_i, is as follows:

$$\theta_{mi} = (1 - p)\theta_i \tag{16}$$

$$\theta_i = \frac{i-1}{pl}\pi, \ (i = 1, 2, 3, \ldots, 2pl) \tag{17}$$

where p is the pole-pair number, θ_i the angle between the ith PM and $\theta = 0$, and l the number of PMs contained in each pole.

Eqs. (16) and (17) are substituted into Eq. (15) to yield:

$$\mathbf{M}_i = \begin{bmatrix} M_{ri} \\ M_{\theta i} \end{bmatrix} = M \begin{bmatrix} \cos\left(\theta - \dfrac{(i-1)(1-p)}{pl}\pi\right) \\ -\sin\left(\theta - \dfrac{(i-1)(1-p)}{pl}\pi\right) \end{bmatrix} \tag{18}$$

The residual magnetization vector of PMs in Halbach array within a cycle $2\pi/p$ is

$$\mathbf{M} = \begin{bmatrix} M_r \\ M_\theta \end{bmatrix} = M \sum_{i=1}^{2l} \begin{bmatrix} \cos\left(\theta - \dfrac{(i-1)(1-p)}{pl}\pi\right) \\ -\sin\left(\theta - \dfrac{(i-1)(1-p)}{pl}\pi\right) \end{bmatrix} \tag{19}$$

$$\theta \in \left(\frac{(2i-1)}{2pl}\pi - \frac{\pi}{pl}, \ \frac{(2i-1)}{2pl}\pi \right], \ (i = 1, 2, 3, \ldots, 2pl).$$

According to the parity of M_r and M_θ, the Fourier series expansion of Eq. (19) in a cycle $2\pi/p$ can be expressed as below:

$$M_r = \frac{M_{r0}}{2} + \sum_{n=1}^{\infty} M_{rn} \cos(np\theta) \tag{20}$$

$$M_\theta = \sum_{n=1}^{\infty} M_{\theta n} \sin(np\theta) \tag{21}$$

where

$$\begin{aligned} M_{r0} &= \frac{1}{\pi/p} \int_{-\pi/p}^{\pi/p} M_r d\theta = \frac{pM}{\pi} \sum_{i=1}^{2l} \int_{\frac{(2i-1)}{2pl}\pi - \frac{\pi}{pl}}^{\frac{(2i-1)}{2pl}\pi} \cos\left[\theta - \frac{(i-1)(1-p)}{pl}\pi\right] d\theta \\ &= \frac{2pM}{\pi} \sin\left(\frac{\pi}{2pl}\right) \sum_{i=1}^{2l} \cos\left[\frac{(1-i)\pi}{l}\right] = 0 \end{aligned} \tag{22}$$

$$\begin{aligned} M_{rn} &= \frac{p}{\pi} \int_{-\pi/p}^{\pi/p} M_r \cos(np\theta) d\theta = \frac{pM}{\pi} \sum_{i=1}^{2l} \int_{\frac{(2i-1)}{2pl}\pi - \frac{\pi}{pl}}^{\frac{(2i-1)}{2pl}\pi} \cos\left[\theta - \frac{(i-1)(1-p)}{pl}\pi\right] \cos(np\theta) d\theta \\ &= \frac{pM}{\pi} \sum_{i=1}^{2l} (A_{1n} - A_{2n}) \end{aligned} \tag{23}$$

$$\begin{aligned} M_{\theta n} &= \frac{p}{\pi} \int_{-\pi/p}^{\pi/p} M_\theta \sin(np\theta) d\theta = -\frac{pM}{\pi} \sum_{i=1}^{2l} \int_{\frac{(2i-1)}{2pl}\pi - \frac{\pi}{pl}}^{\frac{(2i-1)}{2pl}\pi} \sin\left[\theta - \frac{(i-1)(1-p)}{pl}\pi\right] \sin(np\theta) d\theta \\ &= \frac{pM}{\pi} \sum_{i=1}^{2l} (A_{1n} + A_{2n}) \end{aligned} \tag{24}$$

$$A_{1n} = \frac{1}{np+1} \cos\frac{(n+1)(i-1)\pi}{l} \sin\frac{(1+pn)\pi}{2lp} \tag{25}$$

$$A_{2n} = \frac{1}{np-1} \cos\frac{(n-1)(i-1)\pi}{l} \sin\frac{(1-pn)\pi}{2lp} \tag{26}$$

3.3. Analytical Model in the Outer Air Gap

According to the symmetry of the magnetic field, the general solutions of Eqs. (5) and (6) in polar coordinates are as follows:

$$\varphi_1(r,\theta) = \sum_{n=1}^{\infty}\left(C_1 r^{np} + C_2 r^{-np}\right)\cos(np\theta) \tag{27}$$

$$\varphi_2(r,\theta) = \sum_{n=1}^{\infty}\left(C_3 r^{np} + C_4 r^{-np}\right)\cos(np\theta) - \sum_{n=1}^{\infty}\frac{1}{\mu_r}\frac{M_{rn}+npM_{\theta n}}{(np)^2-1}r\cos(np\theta) \tag{28}$$

The coefficients in Eqs. (27) and (28) can be obtained according to Eqs. (9), (10) and the boundary conditions in Eqs. (11)–(14).

$$C_1 = \frac{G_3}{2(G_1R_{mi}^{2np}-1)} - \frac{D_1R_{mo}^{1-np}}{2} \tag{29}$$

$$C_2 = -\frac{R_o^{2np}G_3}{2(G_1R_{mi}^{2np}-1)} + \frac{D_1R_o^{2np}R_{mo}^{1-np}}{2} \tag{30}$$

$$C_3 = \frac{D_1G_1R_{mi}^{np+1}-G_2}{G_1R_{mi}^{2np}-1} \tag{31}$$

$$C_4 = \frac{G_2R_{mi}^{2np}-D_1R_{mi}^{np+1}}{G_1R_{mi}^{2np}-1} \tag{32}$$

where

$$G_1 = \frac{(1+\mu_r)+(1-\mu_r)R_o^{2np}R_{mo}^{-2np}}{(1-\mu_r)R_{mo}^{2np}+(1+\mu_r)R_o^{2np}} \tag{33}$$

$$G_2 = \frac{\left[\left(1+\frac{\mu_r}{np}\right)R_{mo}^{1-np}R_o^{2np} - \left(\frac{\mu_r}{np}-1\right)R_{mo}^{np+1}\right]D_1}{(1-\mu_r)R_{mo}^{2np}+(1+\mu_r)R_o^{2np}} \tag{34}$$

$$G_3 = \left(D_1G_1R_{mi}^{np+1}-G_2\right)(1+\mu_r)+(1-\mu_r)\left(G_2R_{mi}^{2np}-D_1R_{mi}^{np+1}\right)R_{mo}^{-2np} \tag{35}$$

$$D_1 = \frac{M_{rn}+npM_{\theta n}}{[(np)^2-1]\mu_r} \tag{36}$$

Thus, the flux density in the outer air gap can be deduced:

$$B_{1r} = \mu_0H_{1r} = -\mu_0\frac{\partial\varphi_1}{\partial r} = -\mu_0\sum_{n=1}^{\infty}\left[K_1\left(1+R_o^{2np}r^{-2np}\right)r^{np-1}\right]np\cos(np\theta) \tag{37}$$

$$B_{1\theta} = \mu_0H_{1r} = -\frac{\mu_0}{r}\frac{\partial\varphi_1}{\partial\theta} = \frac{\mu_0}{r}\sum_{n=1}^{\infty}K_1\left(1-R_o^{2np}r^{-2np}\right)r^{np}np\sin(np\theta) \tag{38}$$

where

$$K_1 = \frac{G_3-\left(G_1R_{mi}^{2np}-1\right)R_{mo}^{1-np}D_1}{2\left(G_1R_{mi}^{2np}-1\right)} \tag{39}$$

4. ANALYTICAL MODEL IN THE INNER AIR GAP

Unlike in the outer air gap, the magnetic field distribution in the inner air gap does not alternate because two radial magnetized PMs are placed on the bias flux poles of the inner stator. Thus, an improved equivalent magnetic circuit method is adopted to model and analyze the flux density in the inner air gap.

First, the equivalent magnetic circuit models of the PM bias magnetic circuit and the control magnetic circuit are established. Next, the relations between the two fluxes in the inner air gap are derived. Last, the improved analytical model of flux density in the inner air gap is obtained.

4.1. Equivalent Magnetic Circuit Model of the PMs

According to the structural features between the inner stator and the rotor, an equivalent magnetic circuit model of the PM bias magnetic circuit is established, as shown in Fig. 6.

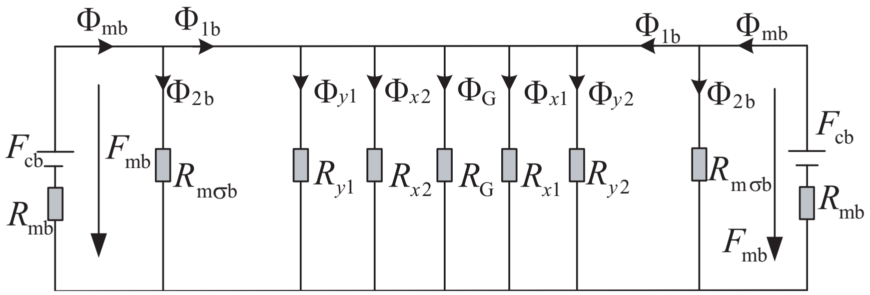

Figure 6. Equivalent magnetic circuit of the PMs.

The material, height and width of the two PMs placed on the flux poles are the same. F_{cb} is the MMF of the two PMs, Φ_{mb} the total flux supplied by a signal PM to the outside, F_{mb} the MMF supplied by a signal PM to the outside, and R_{mb} and $R_{m\sigma b}$ are the internal reluctance and the leakage reluctance of the PM, respectively. Φ_{x1}, Φ_{x2}, Φ_{y1}, Φ_{y2}, and Φ_G are the fluxes flowing through the other five inner stator poles. Φ_{2b} is the leakage flux of the PM; and R_{x1}, R_{x2}, R_{y1}, R_{y2}, and R_G are the reluctances of the air gap in $+x$, $-x$, $+y$, $-y$, and $+G$ directions, respectively.

According to the equivalent magnetic circuits of the PM, the following equations can be obtained:

$$R_{mb} = \frac{h_{mb}}{\mu_0 \mu_r S_{mb}} \tag{40}$$

$$R_{x1} = \frac{x_b}{\mu_0 S_{x1}} \tag{41}$$

$$R_{x2} = \frac{2g_0 - x_b}{\mu_0 S_{x2}} \tag{42}$$

$$R_{y1} = \frac{y_b}{\mu_0 S_{y1}} \tag{43}$$

$$R_{y2} = \frac{2g_0 - y_b}{\mu_0 S_{y2}} \tag{44}$$

$$R_G = \frac{\delta_G}{\mu_0 S_G} \tag{45}$$

where h_{mb} is the magnetization direction length of the PM placed on the inner stator, S_{mb} the section area of the PM, and x_b, y_b, and δ_G are the lengths of inner air gap in $+x$, $+y$, and $+G$ directions, respectively. S_{x1}, S_{x2}, S_{y1}, S_{y2}, and S_G are the areas of poles in $+x$, $-x$, $+y$, $-y$, and $+G$ directions, respectively. The areas of four control poles in this paper are set as follows:

$$S_{x1} = S_{x2} = S_{y1} = S_{y2} = S_b \tag{46}$$

According to Kirchhoff's law of a magnetic circuit and introducing the leakage factor of flux σ_b, the following equations can be obtained:

$$\Phi_{mb} = \frac{F_{cb}\mu_0\mu_r S_{mb}(S_G D_{b1} + 2g_0 S_b D_{b2}\delta_G)}{2\mu_r D_{b1}\delta_G S_{mb} + h_{mb}(S_G D_{b1} + 2g_0 S_b D_{b2}\delta_G)} \tag{47}$$

$$D_{b1} = (2g_0 - x_b)(2g_0 - y_b)x_b y_b \tag{48}$$

$$D_{b2} = -x_b^2 - y_b^2 + 2g_0(x_b + y_b) \tag{49}$$

$$F_{cb} = H_{cb}h_{mb} \tag{50}$$

where H_{cb} is the coercive force of the PM.

Thus, the fluxes of the PMs flowing through the other five inner stator poles are

$$\Phi_{x1} = \frac{1}{\sigma_b} \cdot \frac{\mu_0 F_{mb} S_b}{x_b} \tag{51}$$

$$\Phi_{x2} = \frac{1}{\sigma_b} \cdot \frac{\mu_0 F_{mb} S_b}{2g_0 - x_b} \tag{52}$$

$$\Phi_{y1} = \frac{1}{\sigma_b} \cdot \frac{\mu_0 F_{mb} S_b}{y_b} \tag{53}$$

$$\Phi_{y2} = \frac{1}{\sigma_b} \cdot \frac{\mu_0 F_{mb} S_b}{(2g_0 - y_b)} \tag{54}$$

$$\Phi_G = \frac{1}{\sigma_b} \cdot \frac{\mu_0 F_{mb} S_G}{\delta_G} \tag{55}$$

where F_{mb}=$F_{cb} - R_{mb}\Phi_{mb}$.

4.2. Equivalent Magnetic Circuit Model of the Control Windings

According to the equivalent magnetic circuit method, the equivalent magnetic circuits of the control windings in the x and y directions are established, as shown in Fig. 7. $n_{xb}i_{xb}$ and $n_{xb}i_{xb}$ are the MMF generated by suspension control windings in the x and y directions, respectively. Φ_{xb} and Φ_{yb} are the control fluxes in the x and y directions, respectively.

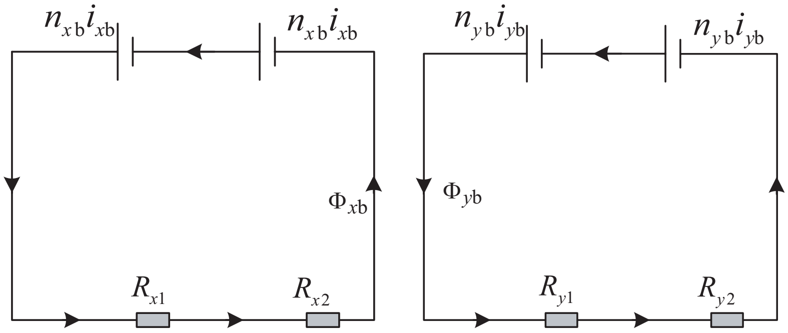

(a) (b)

Figure 7. Equivalent magnetic circuit of the control windings. (a) Equivalent magnetic circuit of the control windings in the x direction. (b) Equivalent magnetic circuit of the control windings in the y direction.

According to Kirchhoff's law of a magnetic circuit and introducing the leakage factor of control flux σ_{cb}, the control flux in the x and y directions can be obtained:

$$\Phi_{xb} = \frac{1}{\sigma_{cb}} \cdot \frac{n_{xb}i_{xb}\mu_0 S_b}{g_0} \tag{56}$$

$$\Phi_{yb} = \frac{1}{\sigma_{cb}} \cdot \frac{n_{yb}i_{yb}\mu_0 S_b}{g_0} \tag{57}$$

4.3. Calculation of the Flux Density in the Inner Air Gap

To simplify the calculation, the leakage factors of the flux in the PMs and the control windings are the same, $\sigma_{cb} = \sigma_b$. According to the flux of the PMs and the control windings deduced in the above section, the total flux flowing though the four suspension control poles are

$$\Phi_{xb1} = \Phi_{x1} + \Phi_{xb} = \frac{\mu_0 S_b}{\sigma_b} \cdot \left(\frac{F_{mb}}{x_b} + \frac{n_{xb} i_{xb}}{g_0} \right) \tag{58}$$

$$\Phi_{xb2} = \Phi_{x2} - \Phi_{xb} = \frac{\mu_0 S_b}{\sigma_b} \cdot \left(\frac{F_{mb}}{2g_0 - x_b} - \frac{n_{xb} i_{xb}}{g_0} \right) \tag{59}$$

$$\Phi_{yb1} = \Phi_{y1} + \Phi_{yb} = \frac{\mu_0 S_b}{\sigma_b} \cdot \left(\frac{F_{mb}}{y_b} + \frac{n_{yb} i_{yb}}{g_0} \right) \tag{60}$$

$$\Phi_{yb2} = \Phi_{y2} - \Phi_{yb} = \frac{\mu_0 S_b}{\sigma_b} \cdot \left(\frac{F_{mb}}{2g_0 - y_b} - \frac{n_{yb} i_{yb}}{g_0} \right) \tag{61}$$

Thus, the corresponding flux density in the inner air gap between the control poles and the rotor are

$$B_{xb1} = \frac{\mu_0}{\sigma_b} \cdot \left(\frac{F_{mb}}{x_b} + \frac{n_{xb} i_{xb}}{g_0} \right) \tag{62}$$

$$B_{xb2} = \frac{\mu_0}{\sigma_b} \cdot \left(\frac{F_{mb}}{2g_0 - x_b} - \frac{n_{xb} i_{xb}}{g_0} \right) \tag{63}$$

$$B_{yb1} = \frac{\mu_0}{\sigma_b} \cdot \left(\frac{F_{mb}}{y_b} + \frac{n_{yb} i_{yb}}{g_0} \right) \tag{64}$$

$$B_{yb2} = \frac{\mu_0}{\sigma_b} \cdot \left(\frac{F_{mb}}{2g_0 - y_b} - \frac{n_{yb} i_{yb}}{g_0} \right) \tag{65}$$

Figure 8 shows the flux density in the air gap and the inner stator when the suspension control currents with the same amplitude and the opposite direction is energized in $+x$ and $-x$ directions. As seen from Fig. 8, there is almost no effect with the air gap flux in the y and G directions when the suspension control currents are energized in the x direction. Similarly, it can be deduced that there is almost no effect with the air gap flux in the x and G directions when the suspension control currents are energized in the y direction. Thus, the flux density in air gap between the eliminating rotor gravity pole and rotor can be deduced:

$$B_G = \frac{1}{\sigma_b} \cdot \frac{\mu_0 F_{mb}}{\delta_G} \tag{66}$$

In addition, the flux density flowing out of the bias pole is

$$B_{mb} = \frac{1}{\sigma_b} \cdot \frac{\Phi_{mb}}{S_{mb}} = \frac{F_{cb} \mu_0 \mu_r (S_G D_{b1} + 2g_0 S_b D_{b2} \delta_G)}{2\sigma_b \mu_r D_{b1} \delta_G S_{mb} + \sigma_b h_{mb} (S_G D_{b1} + 2g_0 S_b D_{b2} \delta_G)} \tag{67}$$

4.4. An Improved Equivalent Magnetic Circuit Model in the Inner Air Gap

The flux density around the poles of the inner stator is uniform based on the formulas derived from the above section because the eccentricity of the rotor is only considered in the x and y directions. However, the reality is that the rotor can be eccentric in any direction, as shown in Fig. 9. The flux density around the poles of the inner stator is not uniform because the air gap widths at any position in the inner stator are not the same. Thus, it is necessary to improve the formulas of the flux density deduced in the above section.

As seen from Fig. 9, $o(0,0)$ is the center of the rotor at the equilibrium position, and $o'(x_0, y_0)$ is the center of the eccentric rotor when an external force is exerted on it. Thus, the eccentric angle of rotor is

$$\alpha = \arctan\left(\frac{y_0}{x_0} \right) \tag{68}$$

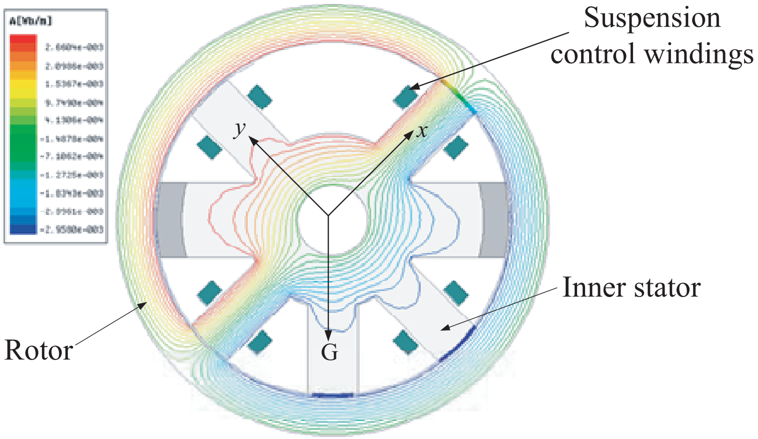

Figure 8. Flux distribution of the energizing suspension control winding in the x direction.

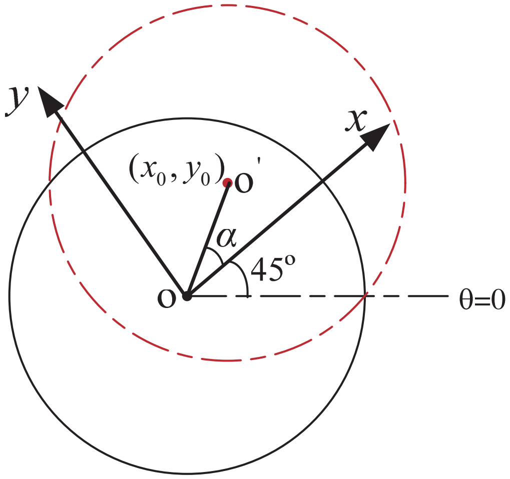

Figure 9. Schematic diagram of the eccentric rotor.

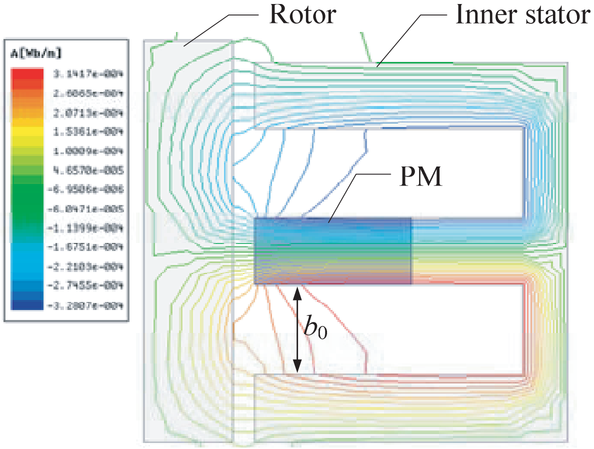

Figure 10. Sketch of the edge effect.

Eccentricity ξ is typically used to indicate the eccentricity of the rotor:

$$\xi = \frac{\sqrt{x_0^2 + y_0^2}}{g_0} \tag{69}$$

Thus, the length of air gap along the circumferential direction of the rotor can be expressed with the mechanical angle θ as follows:

$$g(\theta) = g_0 \left[1+\xi \cos\left(\theta - \alpha - \frac{\pi}{4}\right)\right] \tag{70}$$

where θ is the angle between the optional position of the rotor circumference, and $\theta = 0$.

Thus, the air gap width in Eqs. (62)–(66) are improved as follows:

$$x_b = g_0 \left[1 + \xi \cos\left(\theta_x - \alpha - \frac{\pi}{4}\right)\right] \tag{71}$$

$$y_b = g_0 \left[1 + \xi \cos\left(\theta_y - \alpha - \frac{\pi}{4}\right)\right] \tag{72}$$

$$\delta_G = g_0 \left[1 + \xi \cos\left(\theta_G - \alpha - \frac{\pi}{4}\right)\right] \tag{73}$$

where θ_x, θ_y, and θ_G are the angles between one position of the poles and $\theta = 0$ in the x, y, and G directions, respectively.

The influences of stator slotting and the edge effect are generally not considered when using the equivalent magnetic circuit method. The air gap lengths are regarded as the vertical distances between the poles and rotor by using the formulas deduced by the equivalent magnetic circuit method. Fig. 10 shows the sketch of the edge effect in the GCWMG. As seen from Fig. 10, the air gap length between the middle of a PM pole and the rotor is shorter than the length between the edge of the PM pole and the rotor.

In addition, the approximate length of the actual magnetic circuit in the inner air gap is shown as Fig. 11. δ' is the effective air gap length, θ is the angle between the optional position of rotor circumference and $\theta = 0$, and b_0 is the arc length between two inner stator poles. The amplitude of δ' is varied with the position in inner air gap. In addition, there is an approximately parabolic rate from the minimum length to the maximum length, the effective air gap length is shortest in intermediate of a PM pole, and the air gap length is longest in the center of a stator slot.

The flux density in the middle of two adjacent inner stator poles is set to 0 T because the arc length between two inner stator poles is longer. The arc lengths of the inner stator poles are set l_1, as shown in Fig. 12.

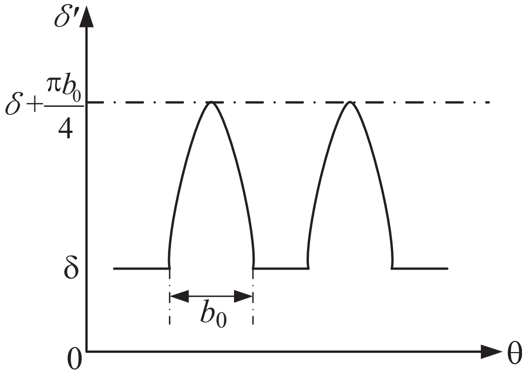

Figure 11. Approximate model of the magnetic circuit in the inner air gap.

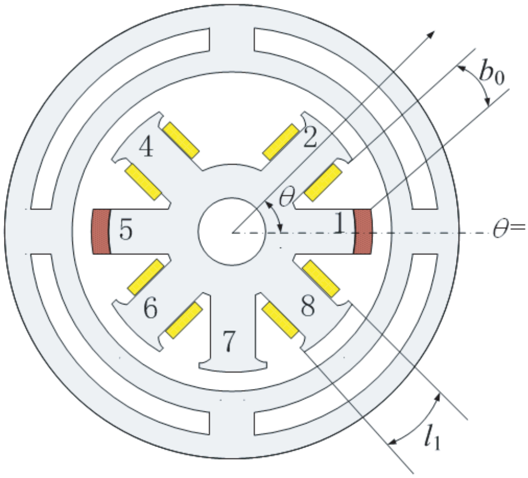

Figure 12. Dimension of the inner stator.

The flux density of the inner air gap can be improved according to the approximate length of the air gap:

$$B_{2n} = \begin{cases} \dfrac{4B_i r^2}{b_0^2}\left[\theta - \dfrac{(2i-3)b_0}{2r} - \dfrac{(2i-3)l_1}{2r}\right]^2 & \theta \in \left[\dfrac{(2i-3)b_0}{2r} + \dfrac{(2i-3)l_1}{2r}, \dfrac{(2i-3)l_1}{2r} + \dfrac{(i-1)b_0}{r}\right) \\ B_i & \theta \in \left[\dfrac{(2i-3)l_1}{2r} + \dfrac{(i-1)b_0}{r}, \dfrac{(2i-1)l_1}{2r} + \dfrac{(i-1)b_0}{r}\right) \\ \dfrac{4B_i r^2}{b_0^2}\left[\theta - \dfrac{(2i-1)l_1}{2r} - \dfrac{(2i-1)b_0}{2r}\right]^2 & \theta \in \left[\dfrac{(2i-1)l_1}{2r} + \dfrac{(i-1)b_0}{r}, \dfrac{(2i-1)l_1}{2r} + \dfrac{(2i-1)b_0}{2r}\right) \end{cases} \tag{74}$$

where i is the identifier of the inner stator pole, which is arranged in anti-clockwise order. To eliminate the self-gravity of rotor, the inner stator adopts an asymmetric structure; therefore, the values of identifier i are set: 1, 2, 4, 5, 6, 7, 8. B_i is the flux density of air gap between the inner stator and rotor, i.e., $B_1 = B_5 = B_{mb}$, $B_2 = B_{xb1}$, $B_4 = B_{yb1}$, $B_6 = B_{xb2}$, $B_7 = B_G$, and $B_8 = B_{yb2}$.

5. VERIFICATION OF THE ANALYTICAL MODELS

To verify the correctness of the derived analytical models, the ANSYS-MAXWELL software which adopts the dispersed form of finite element based on the Maxwell differential equation can translate

Table 1. Main parameters of the GCWMG.

Parameters	Value	Parameters	Value
Power rating (kW)	5	Outer diameter of the rotor $2R_{mo}$ (mm)	218
Rated voltage (V)	180	Numbers of magnets of each pole (l)	2
Rated frequency (Hz)	50	Thickness of PM placed on the inner stator h_{nm} (mm)	15
Rated speed (rpm)	375	Thickness of PM in the Halbach array h_m (mm)	8
Numbers of phases	3	Arc length between the adjacent poles of inner stator b_0 (mm)	55
Material of the silicon steel sheet	DW360-50	Amplitude of the residual flux density B_{rem} (T)	1.35
Numbers of pole-pairs	8	Outer diameter of Region I $2R_o$ (mm)	220
Material of the PM	N42SH	Inner diameter of the rotor $2R_{r2}$ (mm)	142
Outer diameter of the outer stator $2R_s$ (mm)	290	Arc length of poles of the inner stator l_1 (mm)	31.8
Inner diameter of the outer stator $2R_{si}$ (mm)	220	Poles of the inner stator	7

the computation of electromagnetic field into the massive matrix calculations [29]. In this paper the ANSYS-MAXWELL software is used to model the magnetic field in the outer and inner stators. The main design parameters of the GCWMG are given in Table 1. Matlab software is used to compile the corresponding calculation programs for the analytical models of flux density in the outer and inner air gaps. Thus, the analytical model and simulation results obtained by FEA are compared and analyzed.

The wavy cures of the flux density in the radial and tangential directions without considering the effect of slotting in the outer stator are shown in Fig. 13 and Fig. 14. B_{1r} and $B_{1\theta}$ are the components of

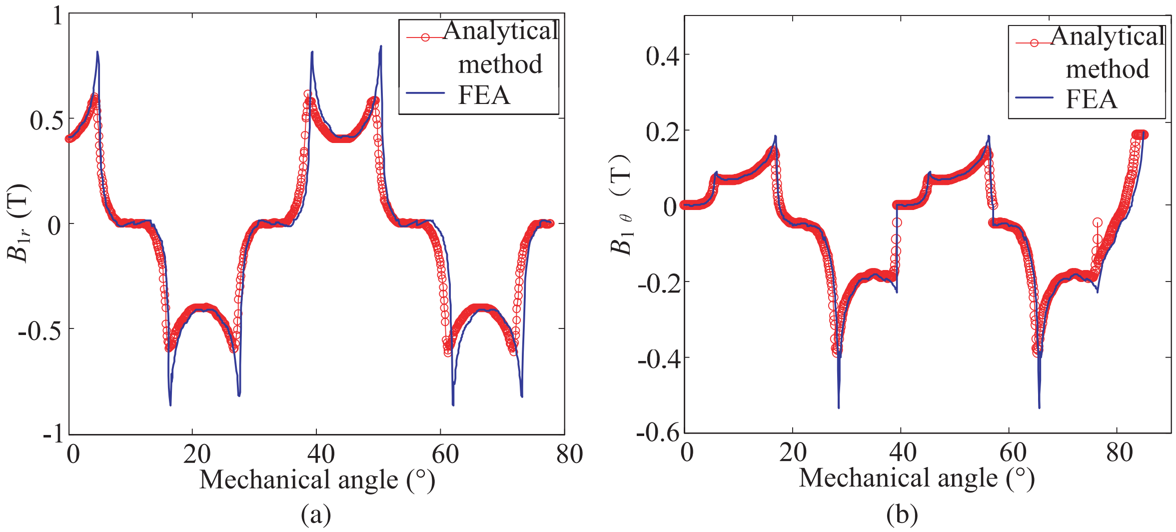

Figure 13. Wavy curves of the flux density in the outer air gap ($r_o = 109.2$ mm). (a) Wavy curve of the flux density in the radial direction. (b) Wavy curve of the flux density in the tangential direction.

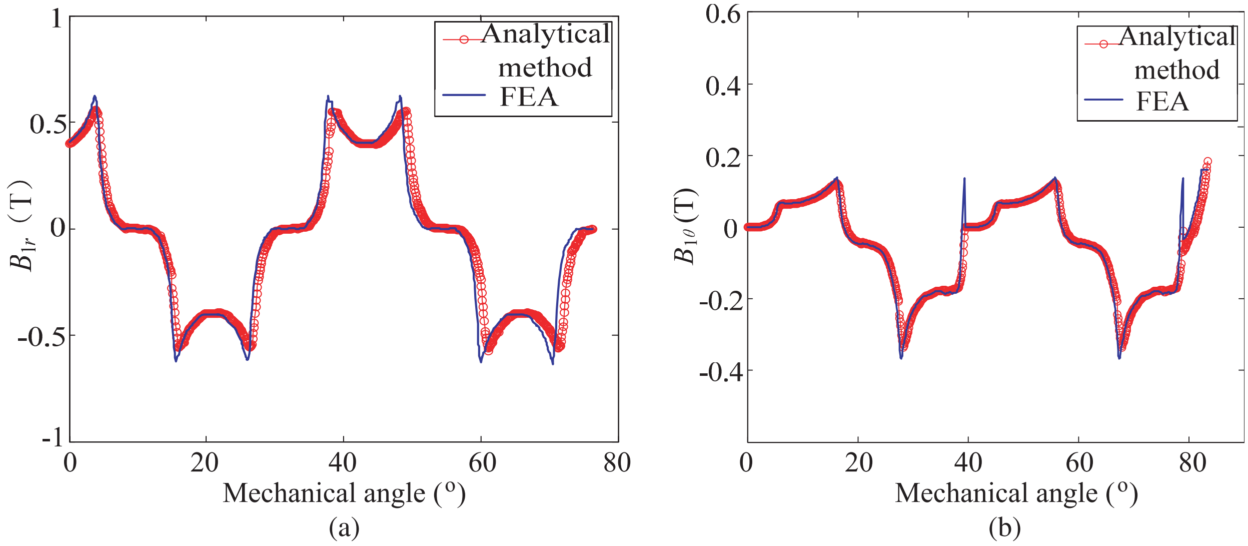

Figure 14. Wavy cures of the flux density in the outer air gap ($r_o = 110\,\mathrm{mm}$). (a) Wavy curve of the flux density in the radial direction. (b) Wavy curve of the flux density in the tangential direction.

flux density in the radial and tangential direction, respectively, when the air gap radius is $r = 109.2\,\mathrm{mm}$ and $r = 110\,\mathrm{mm}$. As seen from the two sets of wave curves in Fig. 13 and Fig. 14, the waveforms predicated by the analytical method proposed in this paper basically coincide with the waveforms simulated using FEA. According to the analysis, the cause of the steep pulse of FEA in Figs. 13 and 14 is the high-frequency harmonics. It is important to note that the values are calculated by analytical model using the Fourier series decomposition method on the basis of ignoring the higher-frequency harmonics. So the two kinds of cures in Figs. 13 and 14 obtained from FEA and analytical model do not coincide with each other at the high-frequency harmonics. The higher of the frequency, the steeper of the pulse obtained from FEA.

To verify the correctness of the improved analytical model in the inner air gap, the amplitudes of the flux density predicted by the improved analytical model and the FEA at $r_{r2} = 70.6\,\mathrm{mm}$ are compared in Fig. 15. Fig. 15(a) shows the amplitude of the flux density in the inner air gap when the rotor is at the central position and no suspension control current is energized. As seen from Fig. 15(a), the flux flowing out of two PMs is flowed into the four suspension control poles and one eliminating rotor gravity pole. In addition, the amplitudes of flux density around the five poles are approximately equal.

Figure 15(b) shows the amplitude of the flux density in the inner air gap when the rotor is at the central position and the suspension control currents are energized. The +200 ampere turns are energized in the $+x$ direction, and the -200 ampere turns are energized in the $-x$ direction. As seen from Fig. 15(b), the amplitude of flux density is decreased in the $+x$ direction and increased in the $-x$ direction. Compared with Fig. 15(a), the magnitudes of flux density corresponding to the other five poles are almost unchanged. Thus, the feasibility of the suspension control in radial 2-DOF is verified.

In the condition of Fig. 15(b), the rotor center is changed from (0 mm, 0 mm) to (0.3 mm, 0.5 mm); the amplitude of the flux density is shown in Fig. 15(c). The lengths of the inner air gap between the surfaces of the poles and the rotor are unequal because of the influence of rotor eccentricity. Thus, the amplitude of flux density around one pole is unequal. As seen from Fig. 15(c), the amplitude of the flux density predicated by the improved analytical method can well fit the amplitude obtained from FEA. Thus, the analytical model predicted by the improved analytical method is correct and reasonable. In addition, an accurate flux density model is provided for the structure design of the GCWMG.

Meanwhile, in order to get a more accurate mathematical model of flux density in inner air gap, the formula of flux density (74) around each pole is divided into three sections. So there are some steep pluses appear when the two formulas in Eq. (74) are switched. For instance, the calculated value of the first formula in Eq. (74) is 1.0923 T when the last sampling point is $\theta = 0.675$. However, the calculated

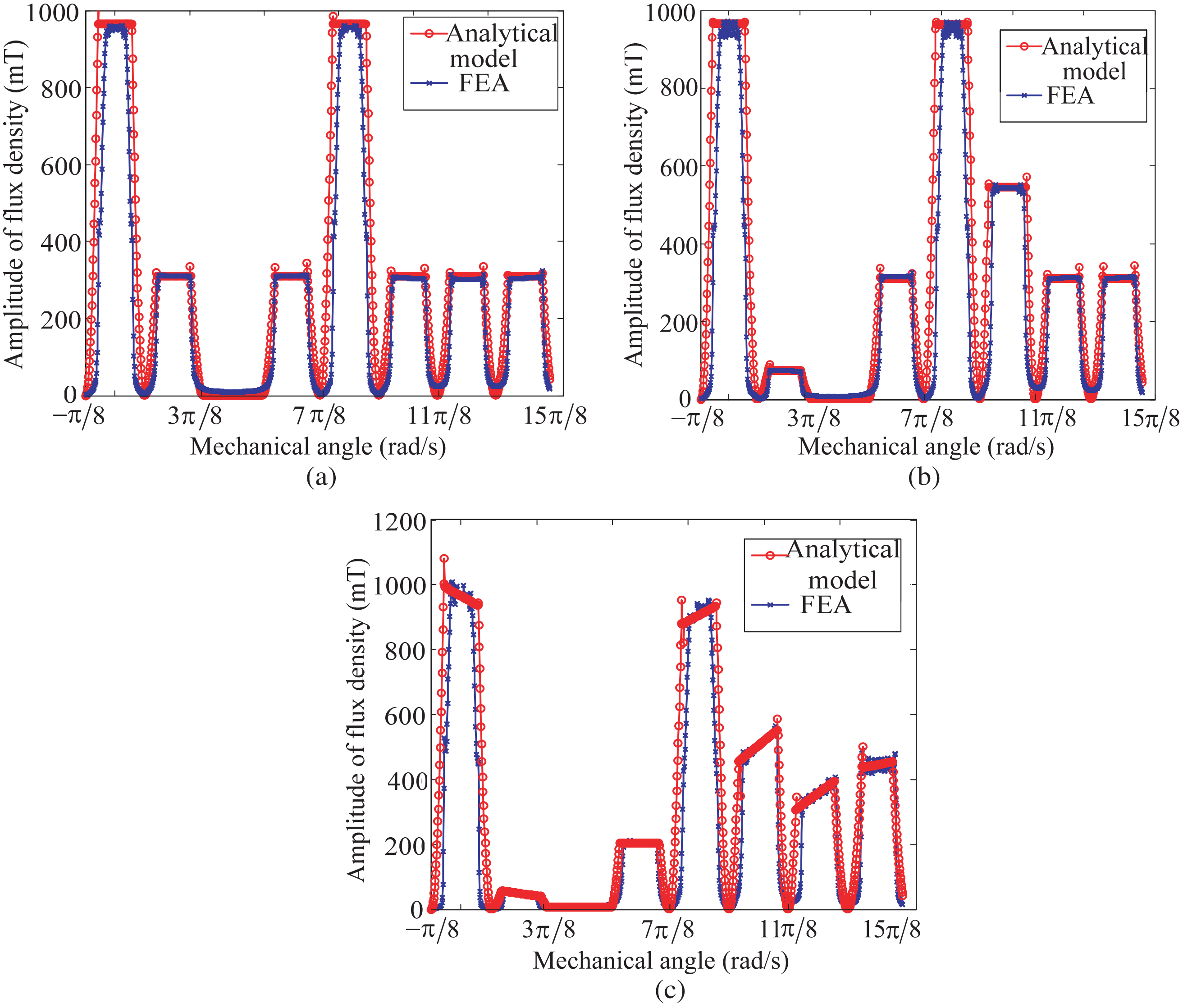

(a) (b) (c)

Figure 15. Amplitude of the flux density in the inner air gap ($r_{r2} = 70.6\,\mathrm{mm}$). (a) Amplitude of the flux density when the rotor is at the central position. (b) Amplitude of the flux density when the suspension control currents are energized. (c) Amplitude of the flux density when the suspension control currents are energized and the rotor is eccentric.

value of the second formula in Eq. (74) is 1.0007 T when the first sampling point is $\theta = 0.676$. And the same situations appear at the other boundaries. To avoid these situations about steep pulses, the more accurate magnetic model which considers the boundary problem specifically will be studied in the future.

The prototype of GCWMB is shown in Fig. 16. To verify the correctness of the analytical model in outer air gap of GCWMG, the Tesla meter is used to measure the flux density in outer air gap of the experimental prototype. The calculated values of analytical model and measured values from a Tesla meter are shown in Fig. 17. Matlab software is used to calculate the flux density of analytical model in outer air gap. As can be seen from Fig. 17, the calculated values and measured values can basically coincide with each other. Then the correctness of the analytical model in outer air gap is further verified.

To verify the correctness of GCWMG, a disturbance experiment is carried out in this paper. The digital control system of rotor supporting along x and y axis in GCWMB is shown in Fig. 18. The control

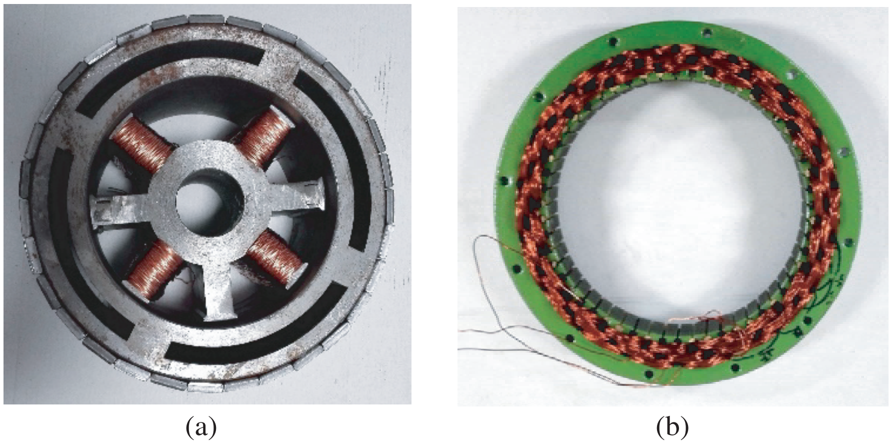
(a) (b)

Figure 16. Prototype of GCWMB. (a) Inner stator and rotor of GCWMB. (b) Stator of GCWMB.

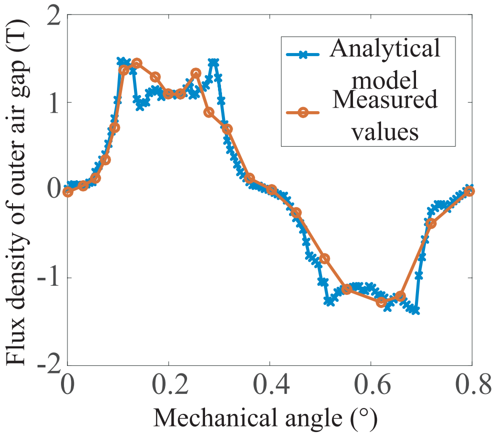

Figure 17. Comparison curves of flux density in outer air gap.

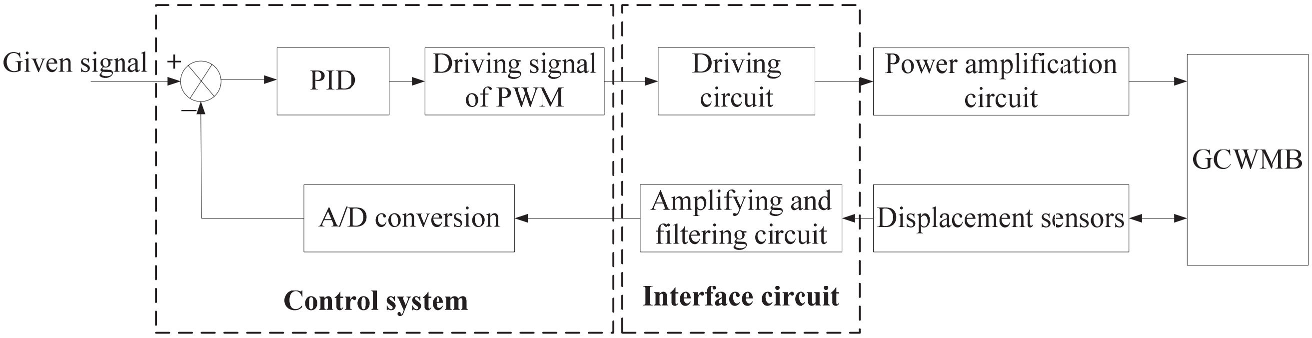

Figure 18. Digital control system of rotor supporting in GCWMB.

system consists of two displacement sensors, PID controller, A/D conversions, driving circuit, amplifying and filtering circuit, etc. The parameter values of PID controller are as follows: $k_p = 5$, $T_i = 0.02\,\mathrm{s}$, $T_d = 0.003\,\mathrm{s}$. In this paper, two eddy current sensors which are installed in the radial x and y directions of GCWMB respectively are used to detect the displacement signals in radial 2-DOF directions. The type of the eddy current sensors used in this digital control system is QH8500. Through the voltage bias circuit, proportional amplification circuit, voltage following circuit and voltage stabilizing circuit,

Figure 19. Displacement waves of rotor at the disturbance test.

the signals collected by displacement sensors can be converted into the voltage recognized by DSP.

The experiment is arranged as follows: when the rotor rotating at the rated speed 375 r/min is stably suspended in the balance position, an external disturbance which can cause an actual displacement in the x direction is added to the shaft, then the displacement of rotor is observed as Fig. 18. In this paper, the external disturbance caused by a wooden hammer striking the side of shaft is a stochastic disturbance.As seen from Fig. 19, the rotor can be suspended stably at the equilibrium position without any disturbances and control currents. When the external disturbance is applied to the rotor in x direction at $t = 0.5\,\text{s}$, the displacement of rotor in x direction is shifted from the equilibrium position. After a short time, the rotor returns back to the balance position using the closed-loop control. Meanwhile, the displacement in G direction are almost unchanged.

6. CONCLUSION

In this paper, a novel GCWMG used for wind turbines is proposed. The GCWMG can not only achieve the suspension and power generation functions but also eliminate the effects of rotor gravity. Because the Halbach magnetized permanent-magnet array is placed outside the rotor, an analytical model based on Fourier series decomposition was developed, taking into account the complex magnetic field distribution of the outer air gap. In addition, taking into account the eccentricity of rotor and edge effects, an improved equivalent magnetic circuit analytical model in inner air gap was developed. Finally, the FEA and experiment results verified the correctness of analytical models in the outer air gap and the inner air gap.

ACKNOWLEDGMENT

This work was supported in part by the Natural Science Foundation of Jiangsu Province (BK 20150510), and by the Priority Academic Program Development of Jiangsu Higher Education Institutions.

REFERENCES

1. Naqvi, A. and H. Ling, "Time-frequency and ISAR characteristics of wind turbines with higher order motions," *Progress In Electromagnetics Research*, Vol. 143, 331–347, 2013.
2. Peng, X., P. Jirutitijaroen, and C. Singh, "A distributionally robust optimization model for unit commitment considering uncertain wind power generation," *IEEE Transactions on Power Systems*, Vol. 32, No. 1, 39–49, 2017.

3. Shokrzadeh, S., M. J. Jozani, and E. Bibeau, "Wind turbine power curve modeling using advanced parametric and nonparametric methods," *IEEE Transactions on Sustainable Energy*, Vol. 5, No. 4, 1262–1269, 2017.
4. Kumbernuss, J., C. Jian, J. Wang, et al., "A novel magnetic levitated bearing system for Vertical Axis Wind Turbines (VAWT)," *Applied Energy*, Vol. 90, No. 1, 148–153, 2012.
5. Yu, Y., H. Zhu, and S. Zeng, "A new self-decoupling magnetic levitation generator for wind turbines," *Progress In Electromagnetics Research M*, Vol. 40, 111–118, 2014.
6. Ren, X., Y. Le, and C. Wang, "Integrated design and optimization method of an asymmetric hybrid thrust magnetic bearing with secondary air-gap," *Progress In Electromagnetics Research B*, Vol. 77, 155–173, 2017.
7. Zheng, S., H. Li, B. Han, and J. Yang, "Power consumption reduction for magnetic bearing systems during torque output of control moment gyros," *IEEE Transactions on Power Electronics*, Vol. 32, No. 7, 5752–5759, 2017.
8. Han, B., Q. Xu, and Q. Yuan, "Multiobjective optimization of a combined radial-axial magnetic bearing for magnetically suspended compressor," *IEEE Transactions on Industrial Electronics*, Vol. 63, No. 4, 2284–2293, 2016.
9. Kanda, K., H. Sasaki, M. Sasaki, and T. Sugiura, "Amplitude reduction of a rotor supported by a superconducting magnetic bearing using nonlinear coupling caused by magnetic force," *IEEE Transactions on Applied Superconductivity*, Vol. 27, No. 4, 3601205, 2017.
10. Yuan, Y., Y. K. Sun, Q. W. Xiang, Y. H. Huang, and Z. Y. Zhu, "Model-free adaptive control for three-degree-of-freedom hybrid magnetic bearings," *Frontiers of Information Technology & Electronic Engineering*, Vol. 18, No. 12, 2035–2045, 2017.
11. Sun, J., Z. Ju, C. Peng, Y. Le, and H. Ren, "A novel 4-DOF hybrid magnetic bearing for DGMSCMG," *IEEE Transactions on Industrial Electronics*, Vol. 64, No. 3, 2196–2204, 2017.
12. Wang, N., Y. Hu, H. Wu, J. Zhang, and C. Song, "Research on forces and dynamics of maglev wind turbine generator," *Journal of Magnetics*, Vol. 18, No. 4, 443–453, 2013.
13. Shrestha, G., H. Polinder, D. J. Bang, and J. A. Ferreira, "Structural flexibility: A solution for weight reduction of large direct-drive wind-turbine generators," *IEEE Transactions on Energy Conversion*, Vol. 25, No. 3, 732–740, 2010.
14. Xie, K., D. Li, R. Qu, and Y. Gao, "A novel permanent magnet vernier machine with Halbach array magnets in stator slot opening," *IEEE Transactions on Magnetics*, Vol. 53, No. 6, 7207005, 2017.
15. Bian, F., W. Zhao, J. Ji, and L. Xu, "Analysis of half Halbach array configurations in linear permanent-magnet vernier machine," *Journal of Magnetics*, Vol. 22, No. 3, 414–422, 2017.
16. Koo, M. M., J. Y. Choi, H. J. Shin, and J. M. Kim, "No-load analysis of PMLSM with Halbach array and PM overhang based on three-dimensional analytical method," *IEEE Transactions on Applied Superconductivity*, Vol. 26, No. 4, 2016.
17. Salihu, S. M., N. Misron, N. Mariun, M. L. Othman, and T. Hanamoto, "A novel double-stator permanent magnet generator integrated with a magnetic gear," *Progress In Electromagnetics Research M*, Vol. 49, 69–80, 2016.
18. Wang, Q., S. Niu, and S. Yang, "Design optimization and comparative study of novel magnetic-geared permanent magnet machines," *IEEE Transactions on Magnetics*, Vol. 53, No. 6, 8104204, 2017.
19. Li, H. and H. Zhu, "Design of bearingless flux-switching permanent-magnet motor," *IEEE Transactions on Applied Superconductivity*, Vol. 26, No. 4, 2016.
20. Peng, W., Z. Xu, D. H. Lee, and J. W. Ahn, "Control of radial force in double stator type bearingless switched reluctance motor," *Journal of Electrical Engineering and Technology*, Vol. 8, No. 4, 766–772, 2013.
21. Smeets, J. P. C., T. T. Overboom, J. W. Jansen, and E. A. Lomonova, "Three-dimensional analytical modeling technique of electromagnetic fields of air-cored coils surrounded by different ferromagnetic boundaries," *IEEE Transactions on Magnetics*, Vol. 49, No. 12, 5698–5708, 2013.

22. Kremers, M. F. J., J. J. H. Paulides, and E. A. Lomonova, "Toward accurate design of a transverse flux machine using an analytical 3-D magnetic charge model," *IEEE Transactions on Magnetics*, Vol. 51, No. 11, 2015.
23. Jian, L., G. Xu, C. C. Mi, K. T. Chau, and C. C. Chan, "Analytical method for magnetic field calculation in a low-speed permanent-magnet harmonic machine," *IEEE Transactions on Energy Conversion*, Vol. 26, No. 3, 862–870, 2011.
24. Santra, T., D. Roy, and S. Yamada, "Calculation of force between two ring magnets using adaptive montecarlo technique with experimental verification," *Progress In Electromagnetics Research M*, Vol. 49, 181–193, 2016.
25. Özkaya, N., D. Leger, D. Goldsheyder, and M. Nordin, "Stress and strain," *Fundamentals of Biomechanics*, Springer International Publishing, 2017.
26. Yu, Y., W. Zhang, Y. Sun, and P. Xu, "Basic characteristics and design of a novel hybrid magnetic bearing for wind turbines," *Energies*, Vol. 9, No. 11, 2016.
27. Le, Y., J. Sun, and B. Han, "Modeling and design of 3-DOF magnetic bearing for high-speed motor including eddy-current effects and leakage effects," *IEEE Transactions on Industrial Electronics*, Vol. 63, No. 6, 3656–3665, 2016.
28. Santra, T., D. Roy, and A. Bikash Choudhury, "Calculation of passive magnetic force in a radial magnetic bearing using general division approach," *Progress In Electromagnetics Research M*, Vol. 54, 91–102, 2017.
29. Martyanov, A. S. and N. I. Neustroyev, "ANSYS Maxwell software for electromagnetic field calculations," *Eastern European Scientific Journal*, Vol. 5, 2014.